Supplementary Information for

Unconventional Catalytic Kinetics of Dual Field Regulated Pyrochlore-type High-entropy Ceramics towards Li2S4 Intermediate

Lin Zhou[1], Handing Liu[2,*], Ji-Xuan Liu [1], Xinrui Zhang[2], Yixi Yao[2], Ruirui Wang[3], Ziliang Chen[4,*], Prashanth W. Menezes [5,*], and Guo-Jun Zhang[1,*]

Correspondence to: liuhd@ier.org.cn; zlchen@suda.edu.cn;

prashanth.menezes@mailbox.tu-berlin.de; gjzhang@dhu.edu.cn.

Table S1. Comparison of electrochemical performances of HEZO-S electrode with previously reported metal oxide or carbon-based cathodic material.

Products	Electrode formulation[a]	Capacity for first cycle (A/B)	Cycling stability (A/B/*n*)[b]	Ref.
$(Ni_{0.2}Co_{0.2}Cu_{0.2}Mg_{0.2}Zn_{0.2})O$	70:30	1244/0.2	784/0.2/500	[S1]
CoNiCuMnZnFe-PBA	70:20:10	1335/0.1	571/0.1/200	[S2]
$La_{0.8}Sr_{0.2}(Cr_{0.2}Mn_{0.2}Fe_{0.2}Co_{0.2}Ni_{0.2})O_3$	70:20:10	1218/0.2	714/1/200	[S3]
CC/ (Fe, Co, Ni, Mn, Cr) O	80:10:10	1294/0.1	458/2/1000	[S4]
HE-O_x	80:20	1224/0.2	919/0.2/100	[S5]
Polymeric zwitterion	80:10:10	1279/0.2	808/1/1000	[S6]
$La_{0.8}Sr_{0.2}MnO_3$	80:13:7	920/0.1	510/0.1/150	[S7]
Eugenol phosphazene	70:20:10	958/0.2	392/0.5/200	[S8]
Nb_4N_5–Nb_2O_5	80:10:10	1354/0.5	856/2/1000	[S9]
$Sr_{0.9}Ti_{1-x}Mn_xO_{3-\delta}$	70:20:10	1313/0.2	634/1/500	[S10]
In_2O_{3-x} @C	/	1190/0.2	872/3/500	[S11]
S/Co-V_2O_5	70:20:10	1168/0.3	630/5/300	[S12]
A/R-TiO_2	80:10:10	1210/0.1	946/1/100	[S13]
ZrO_{2-x}/CNTs-OH	/	1240/0.1	~670/3/1000	[S14]
$W_{18}O_{49}$	70:20:10	1234/0.2	600/2/1000	[S15]
Co@CoO_{1-x}	70:20:10	1167/0.1	527/2/400	[S16]
$(CrMnFeNiMg)_3O_4$	80:10:10	857/0.1	552/0.5/300	[S17]
CoFeMnO	60:30:10	1082/0.2	952/1/600	[S18]
δ-MnO_2 nanosheets	80:10:10	1377/0.1	698/1/500	[S19]
HEZO-S	**70:20:10**	**1507/0.1**	**1238/0.1/150 667/0.5/4000**	**This work**

[a]Weight ratio of the active material, carbon and binder. PVDF was used as a binder. Other values used were specified.
[b]A/B/*n* means the capacity of A (mAh g^{-1}) remained after *n* cycles at the certain current density of B (C).

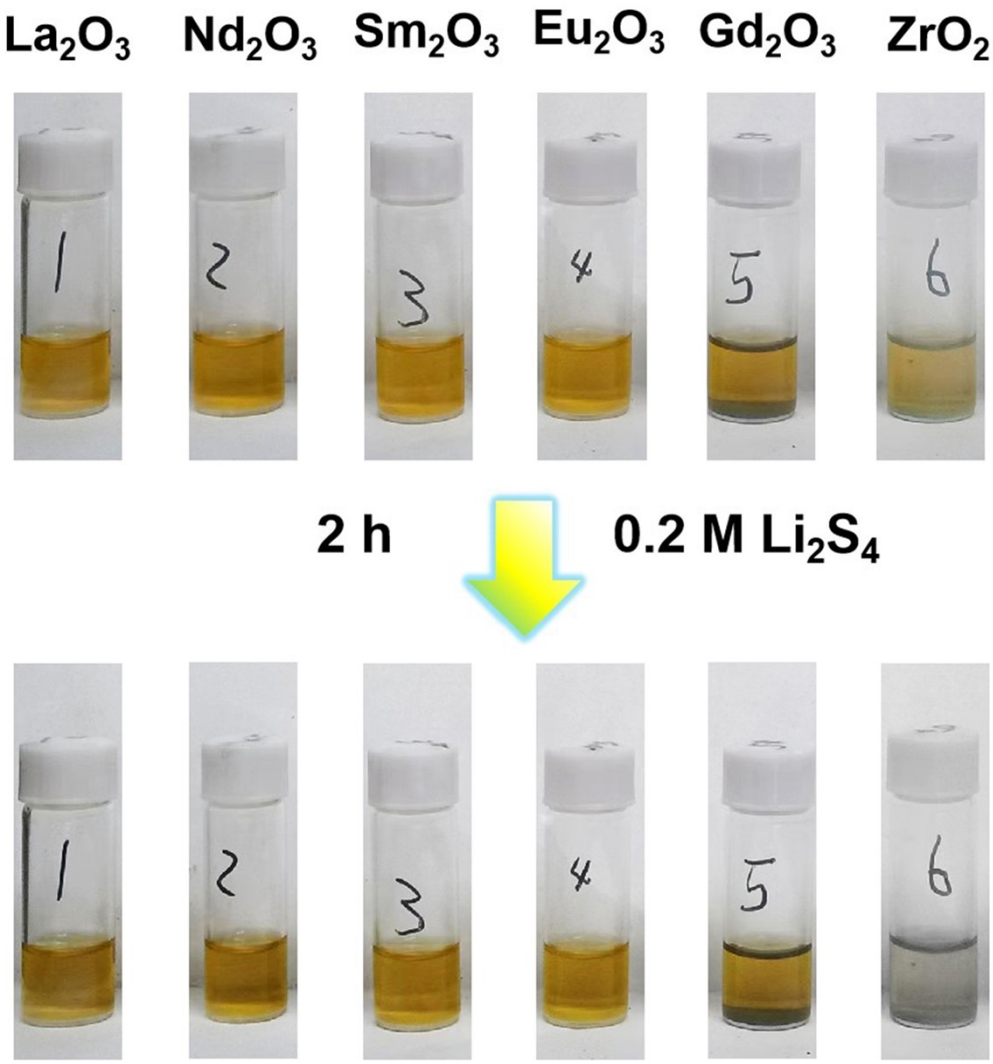

Figure S1. Adsorption experiment of La_2O_3, Nd_2O_3, Sm_2O_3, Eu_2O_3, Gd_2O_3, and ZrO_2 coated PP separator.

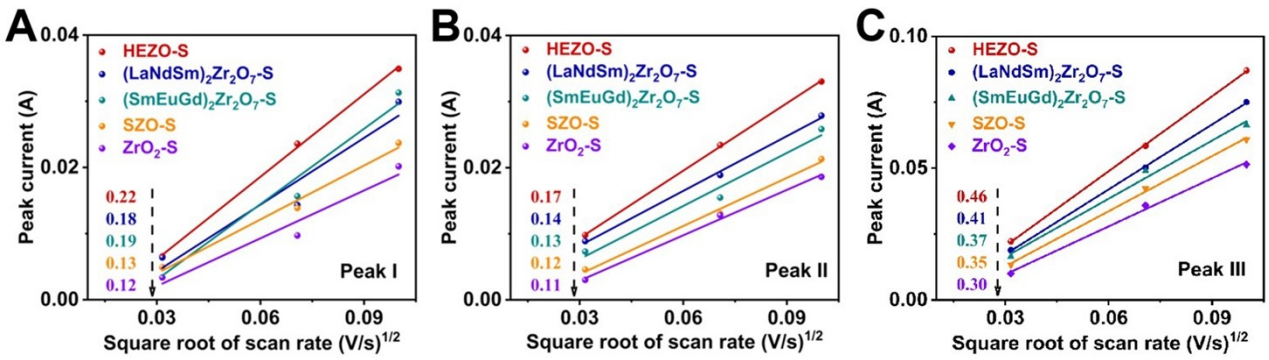

Figure S2. A, Current linear fitting curves and D_{Li+} values of Peak I. **B**, Current linear fitting curves and D_{Li+} values of Peak II. **C**, Current linear fitting curves and D_{Li+} values of Peak III.

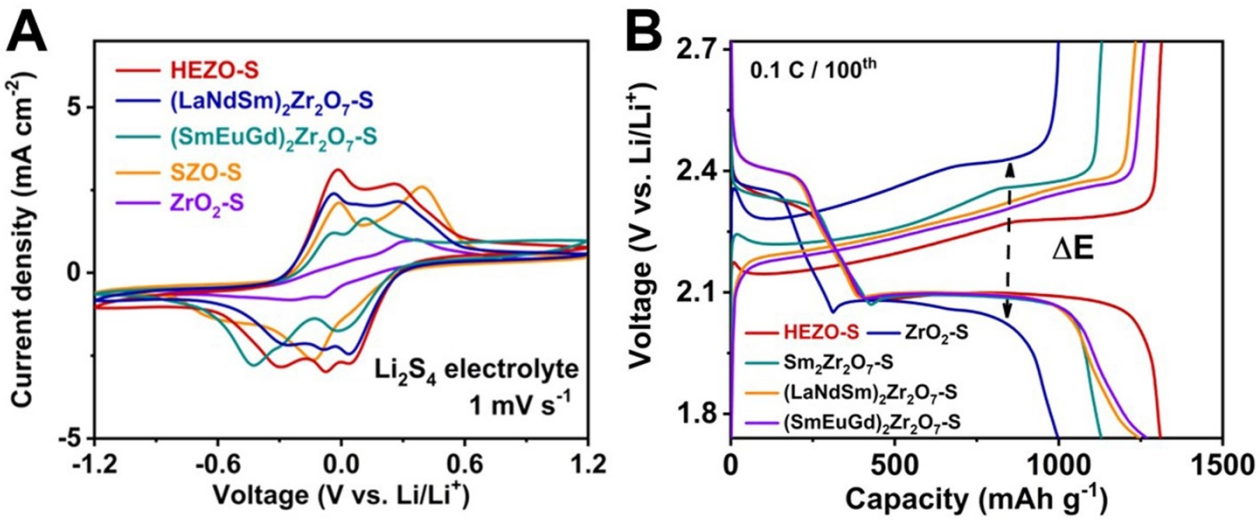

Figure S3. A, CV curves of Li_2S_4 catholyte symmetric cells for HEZO / Li_2S_4/ HEZO, $(LaNdSm)_2Zr_2O_7$ / Li_2S_4/ $(LaNdSm)_2Zr_2O_7$, $(SmEuGd)_2Zr_2O_7$ / Li_2S_4/ $(SmEuGd)_2Zr_2O_7$, $Sm_2Zr_2O_7$ / Li_2S_4/ $Sm_2Zr_2O_7$, and ZrO_2 / Li_2S_4/ ZrO_2 electrodes. **B**, Galvanostatic discharge-charge curves of different cycle numbers at 0.1 C with HEZO-S, $(LaNdSm)_2Zr_2O_7$-S, $(SmEuGd)_2Zr_2O_7$-S, $Sm_2Zr_2O_7$-S, and ZrO_2-S.

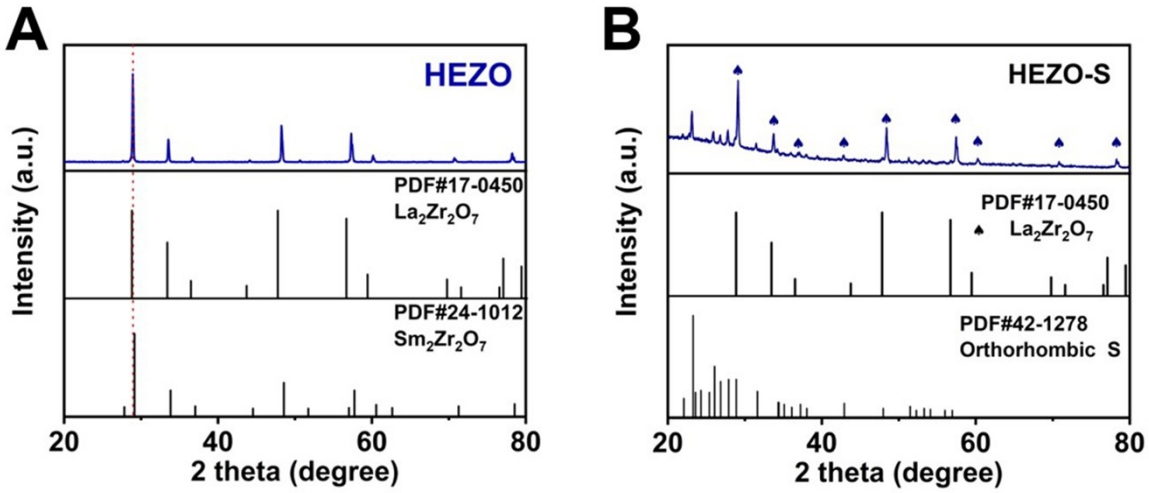

Figure S4. XRD spectra of HEZO-S, and Standard pdf card of $La_2Zr_2O_7$, $Sm_2Zr_2O_7$, and S.

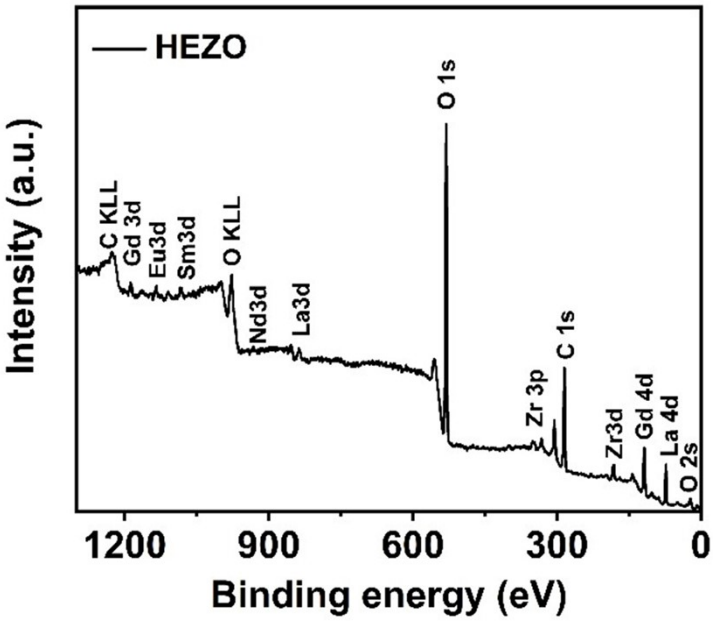

Figure S5. High-resolution full spectra of HEZO.

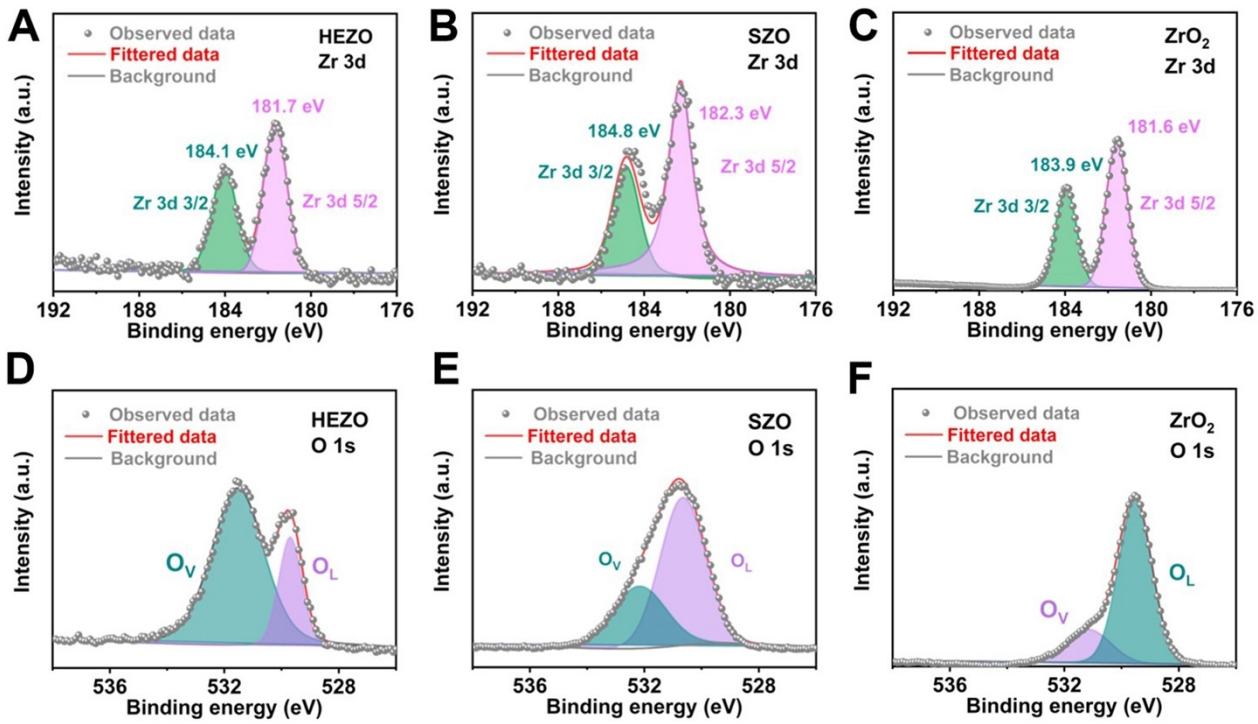

Figure S6. High-resolution full spectra. **A−C,** Zr 3d spectra of HEZO, $Sm_2Zr_2O_7$, and ZrO_2. **D−F,** O 1s spectra of HEZO, $Sm_2Zr_2O_7$, and ZrO_2.

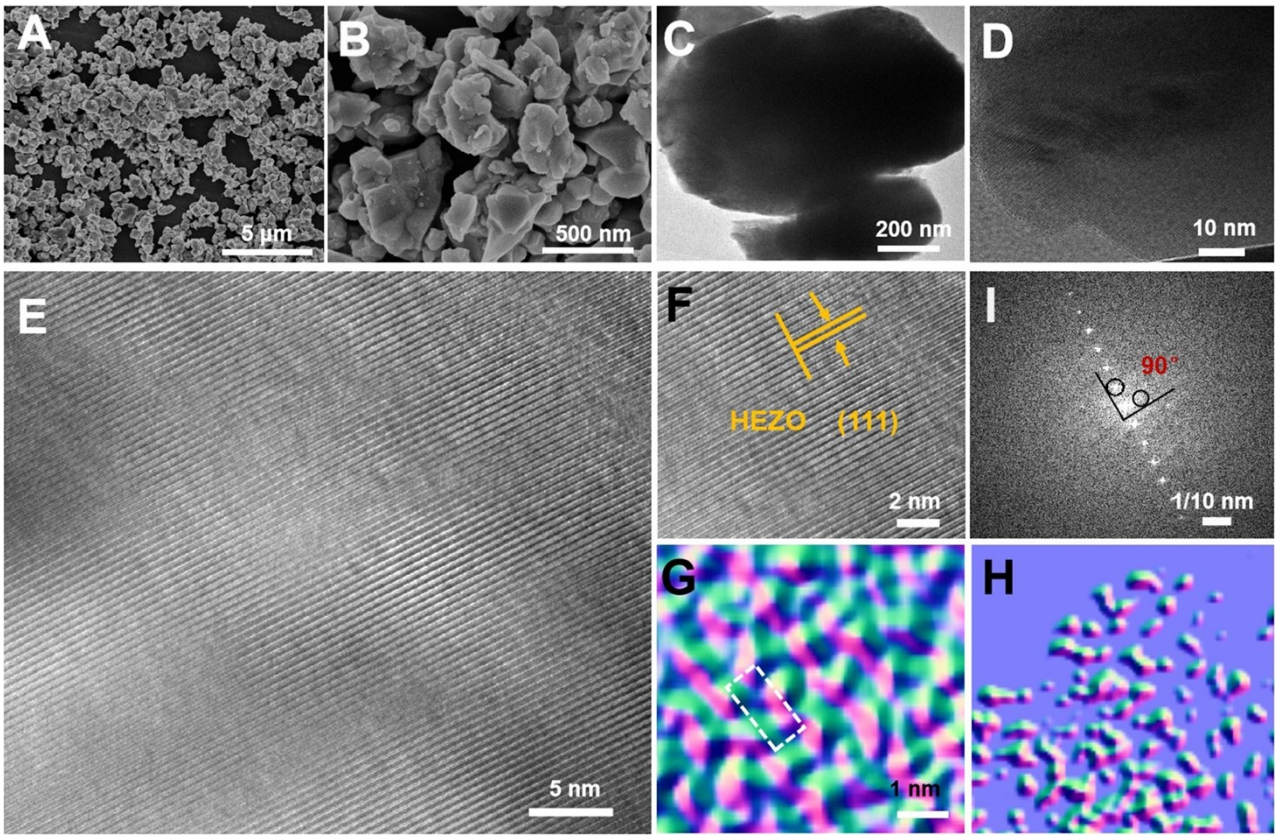

Figure S7. A−D, FESEM images of HEZO. **E−F,** HRTEM images of HEZO. The three-dimensional AOGF mapping corresponding to the magnified high-resolution spherical aberration electron microscope image of **G,** $Sm_2Zr_2O_7$, **H**, HEZO. **I,** Inverse FFT of HRTEM images.

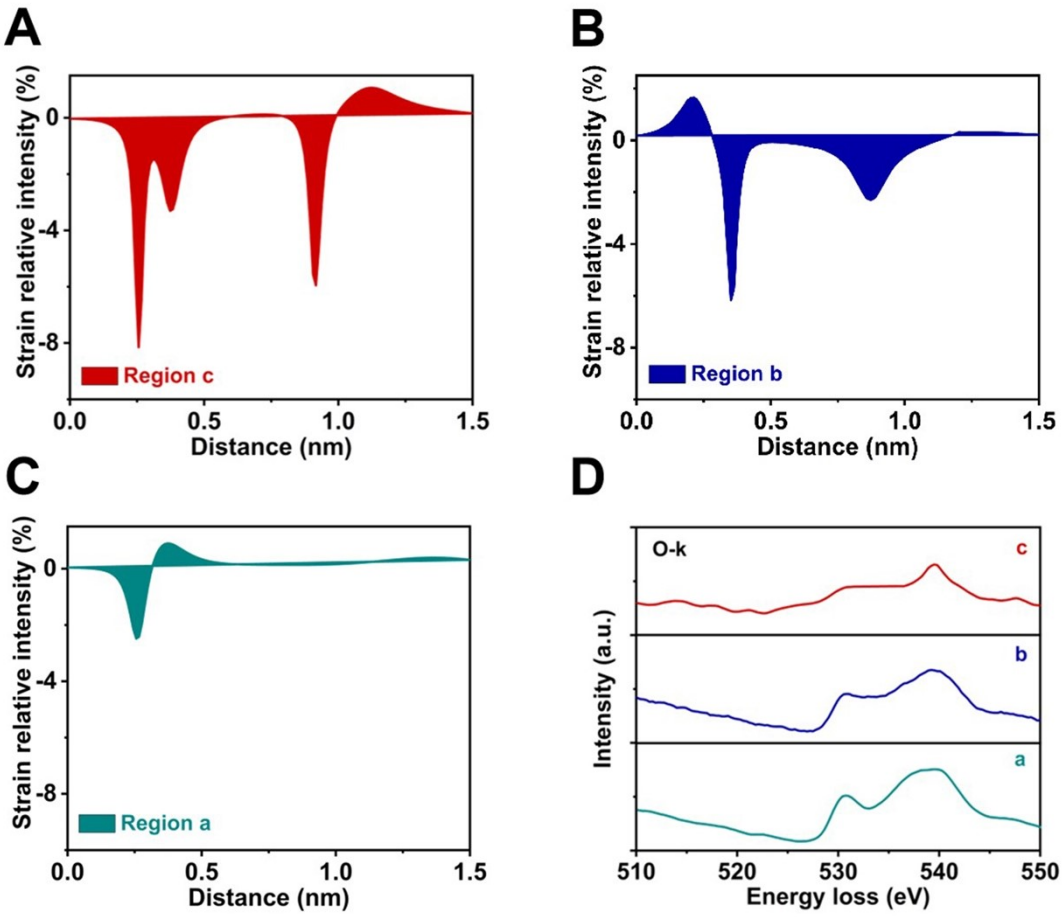

Figure S8. Cumulative stress intensity in a 1.5 nm width region along the heterogeneous interface (>0 for tensile stress, <0 for compressive stress) of HEZO, **A,** c region of Fig. 2l, **B,** b region of Fig. 2l, **C,** a region of Fig. 2l. **D**, Oxygen K-edges of the EELS spectra acquired from the regions in the inset of TEM image of a, b, c, region.

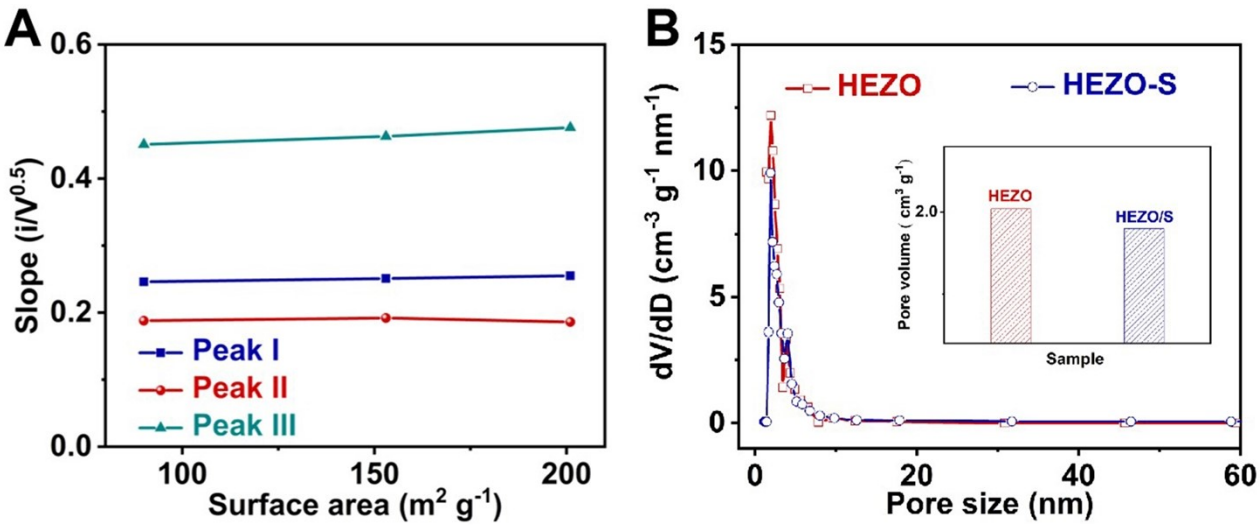

Figure S9. A, The D_{Li+} value of the peak value of the linear fitting curve varies with the specific surface area. **B,** The aperture distribution of HEZO, the embedded small plot is the pore volume.

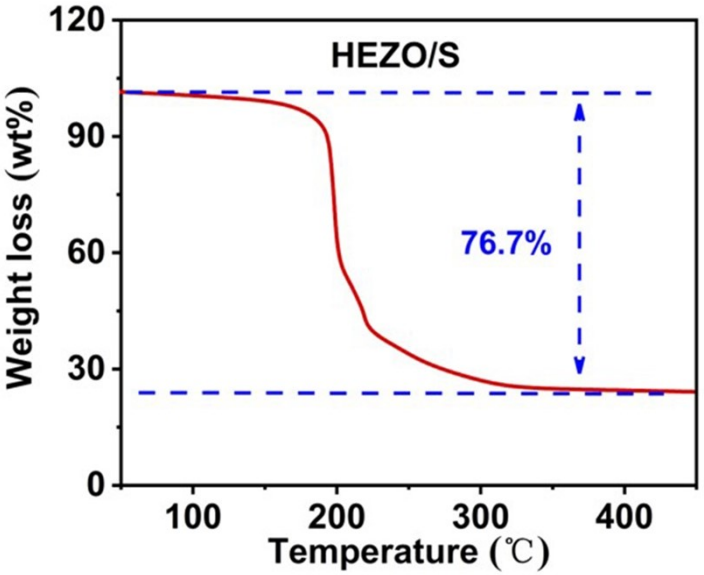

Figure S10. Sulfur content of HEZO-S by TGA measured under N_2 atmosphere from room temperature to 800 ℃ with a heating rate of 10 ℃ min^{-1}.

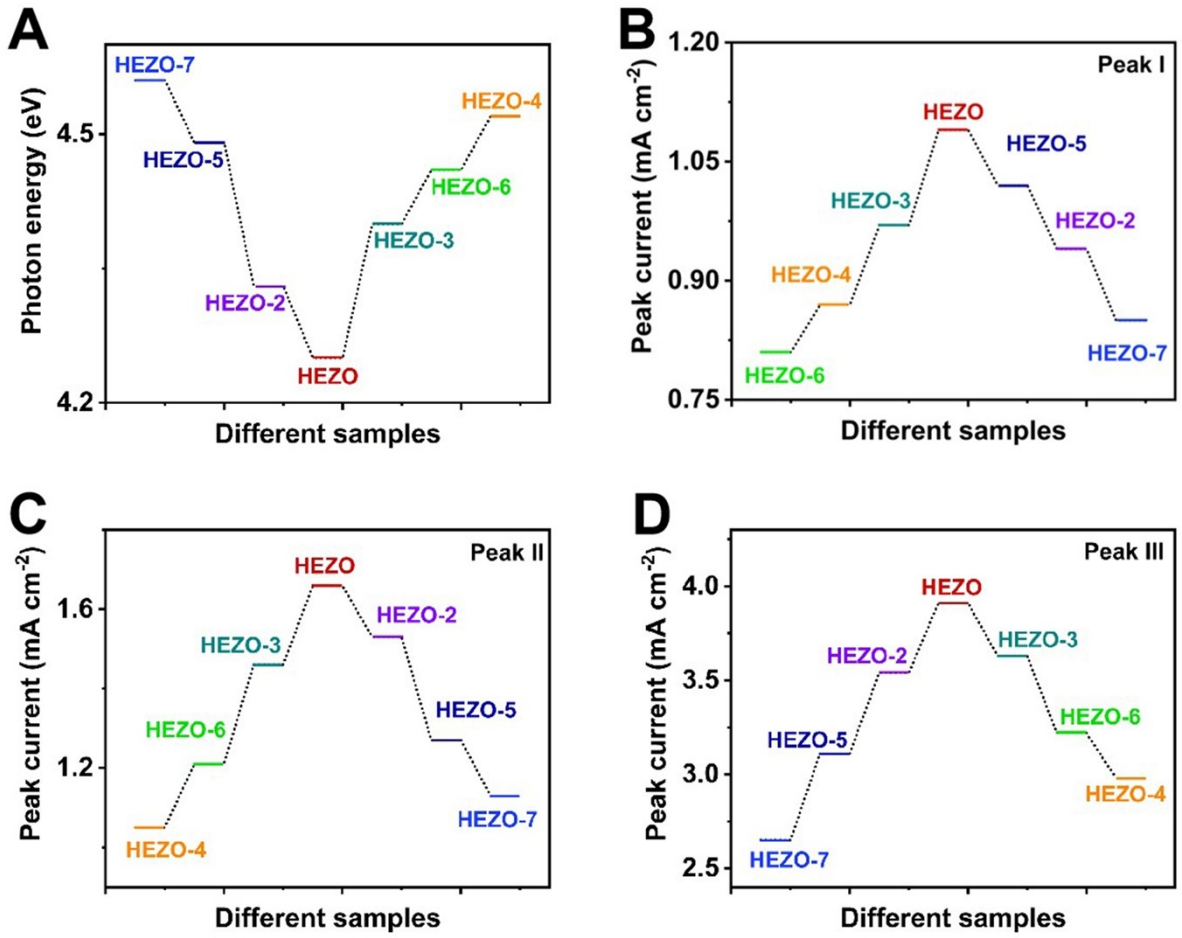

Figure S11. HEZO, HEZO-2, HEZO-3, HEZO-4, HEZO-5, HEZO-6, HEZO-7 of **A,** band gap sizes, **B,** the current intensity of characteristic peak I, **C,** the current intensity of characteristic peak II, **D,** the current intensity of characteristic peak III.

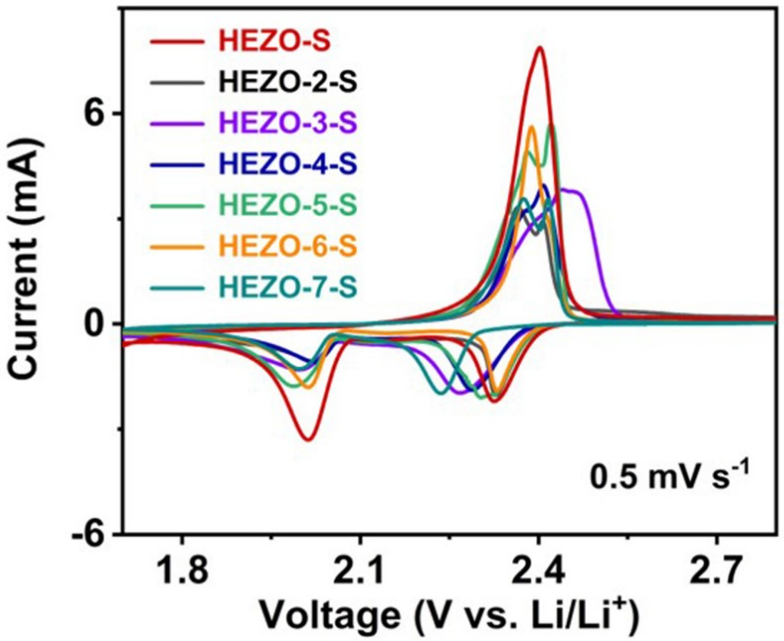

Figure S12. CV curves of HEZO-S, HEZO-2-S, HEZO-3-S, HEZO-4-S, HEZO-5-S, HEZO-6-S, HEZO-7-S cathodes.

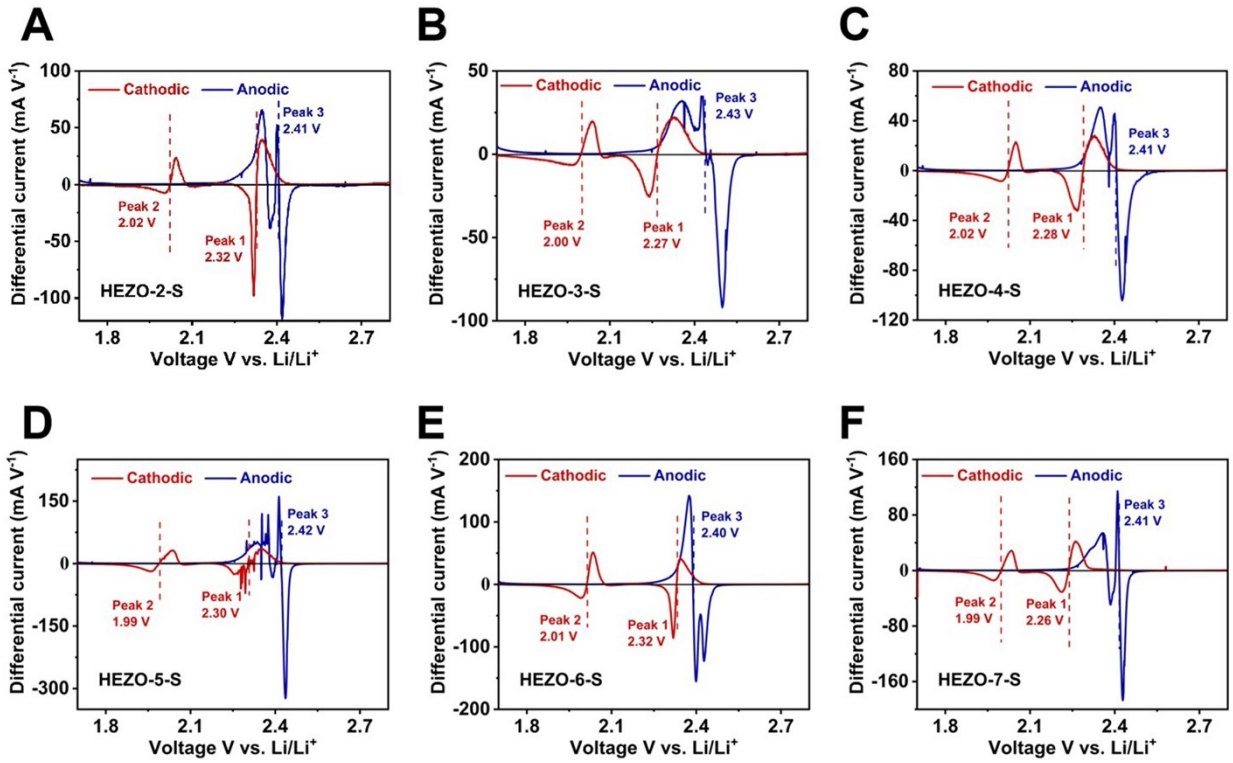

Figure S13. A, Differential CV curves of HEZO-2-S. **B,** Differential CV curves of HEZO-3-S. **C,** Differential CV curves of HEZO-4-S. **D,** Differential CV curves of HEZO-5-S. **E,** Differential CV curves of HEZO-6-S. **F,** Differential CV curves of HEZO-7-S.

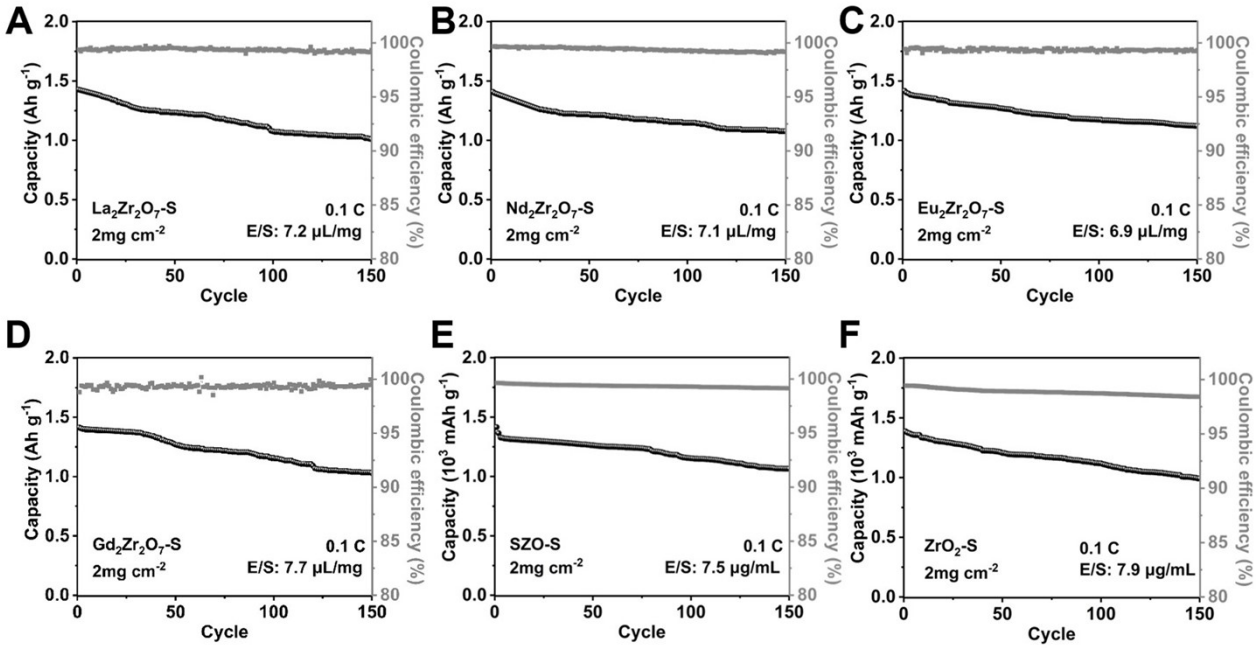

Figure S14. Long-cycling performance at 0.1 C of **A,** $La_2Zr_2O_7$-S, **B,** $Nd_2Zr_2O_7$-S, **C,** $Eu_2Zr_2O_7$-S, **D,** $Gd_2Zr_2O_7$-S, **E,** $Sm_2Zr_2O_7$-S, **F,** ZrO_2-S.

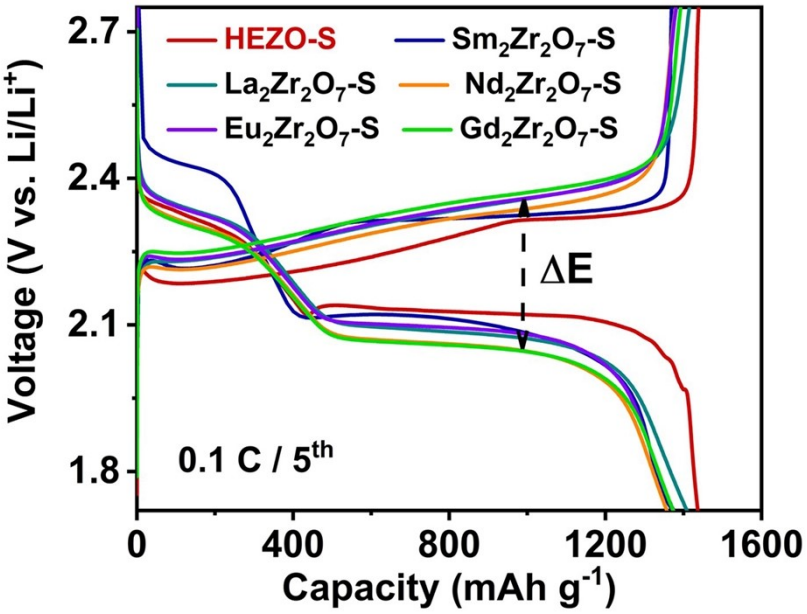

Figure S15. Different samples for discharge/charge curve at 0.1 C after 5th cycles.

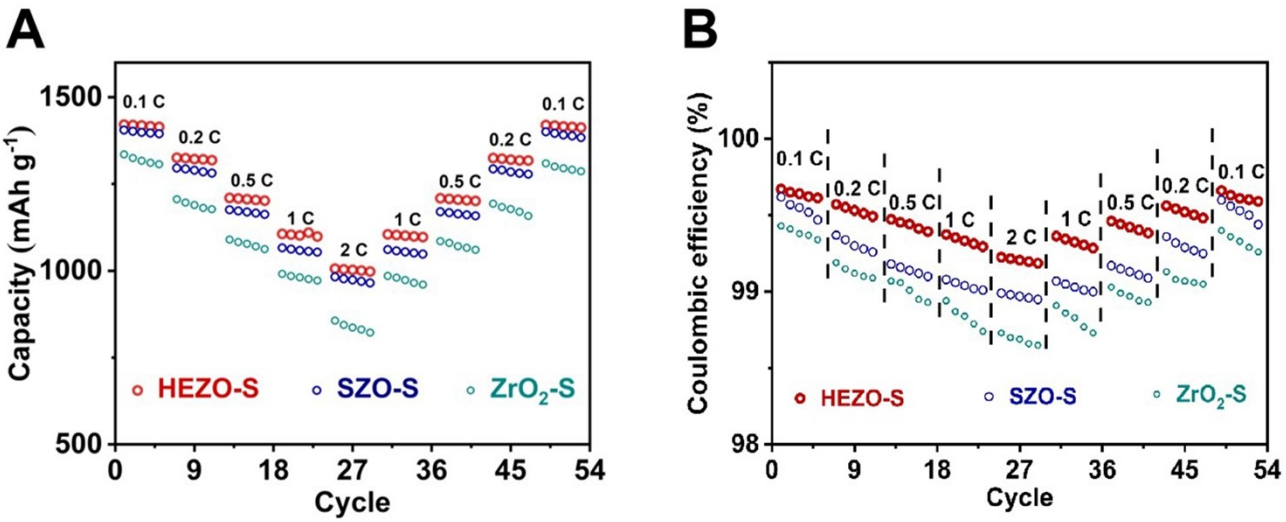

Figure S16. Rate capabilities from 0.1 C to 2 C of **A,** $Sm_2Zr_2O_7$-S, **B,** ZrO_2-S.

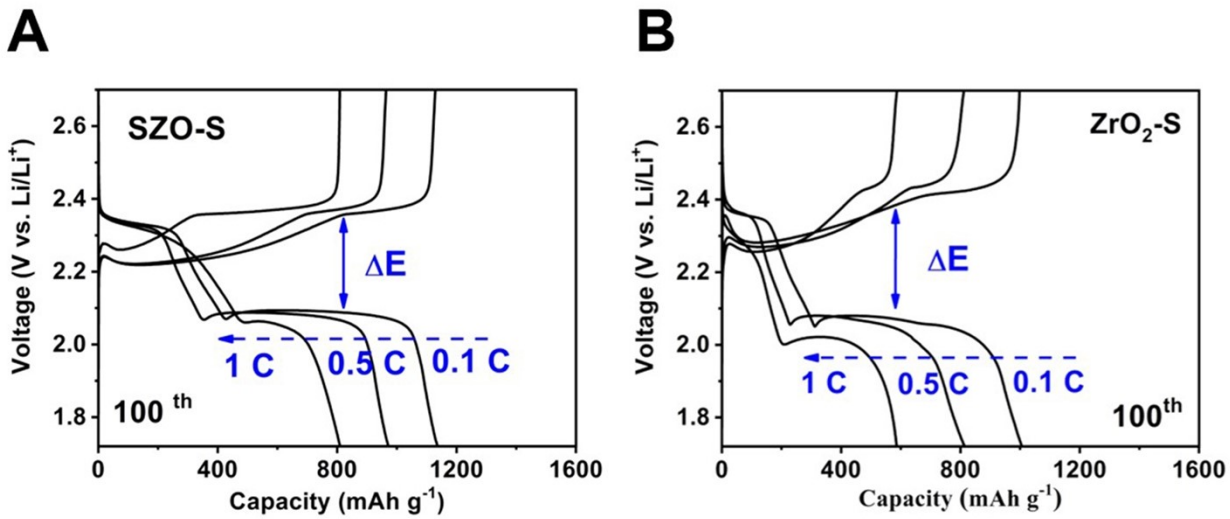

Figure S17. Different rates (0.1 C, 0.5 C, and 1 C) for discharge/charge curve of **A,** $Sm_2Zr_2O_7$-S, **B,** ZrO_2-S after 100 cycles.

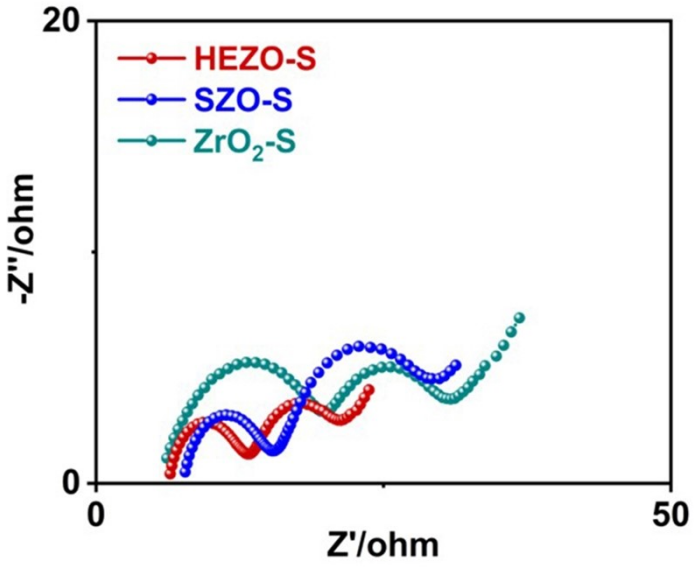

Figure S18. EIS of HEZO-S, $Sm_2Zr_2O_7$-S, and ZrO_2-S cathodes under room temperature.

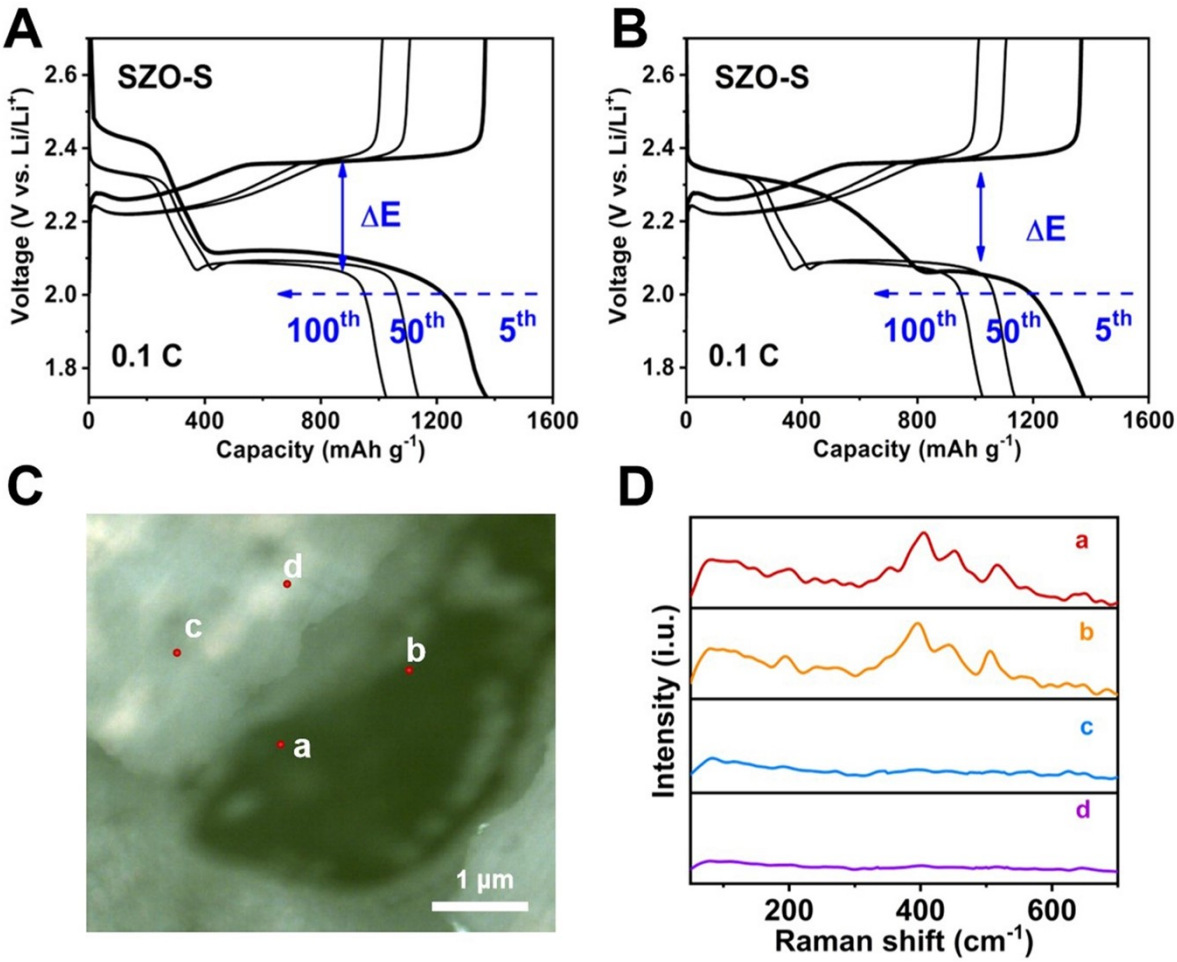

Figure S19. A, Different cycles (5th, 50th, and 100th) for discharge/charge curve of $Sm_2Zr_2O_7$-S at 0.1 C without 532 nm laser. **B,** Different cycles (5th, 50th, and 100th) for discharge/charge curve of $Sm_2Zr_2O_7$-S at 0.1 C without 532nm laser. **C**, Raman image of high-magnification objective lens at a discharge depth of 10%. **D**, Raman characteristic peak signals in different regions.

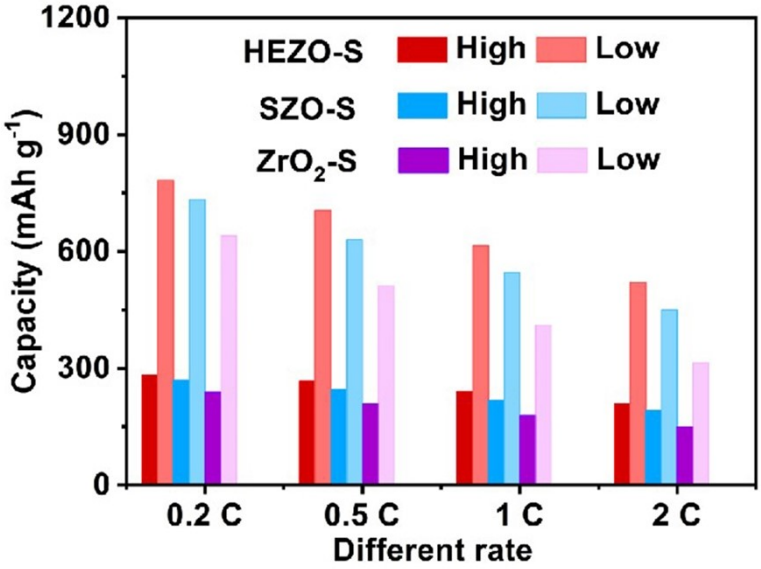

Figure S20. Contribution value of high and low potential platform capacity of HEZO-S, $Sm_2Zr_2O_7$-S ZrO_2-S electrode under different current densities.

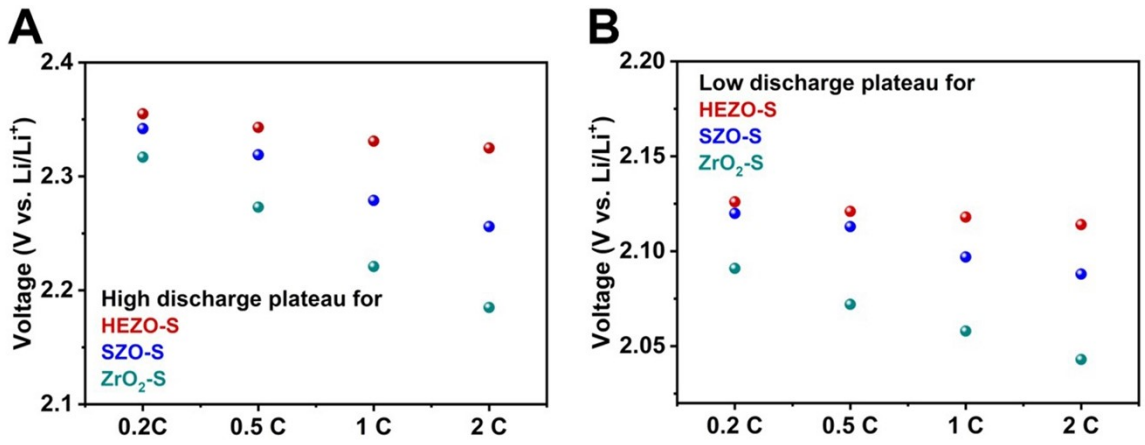

Figure S21. A, High discharge plateau voltage and **B,** low discharge plateau voltage of HEZO-S, $Sm_2Zr_2O_7$-S, ZrO_2-S cathodes at different C (0.2, 0.5, 1, 2) rates.

Figure S21 shows the high and low discharge plateau voltages of HEZO-S, $Sm_2Zr_2O_7$-S ZrO_2-S electrodes at different C-rates. Low discharge plateau voltage of HEZO-S was 2.126, 2.121, 2.118, and 2.114 V at 0.2 C, 0.5 C, 1 C, and 2 C, respectively, while high discharge plateau voltage was 2.355, 2.343，2.331， and 2.325 V, respectively. Low discharge plateau voltage of $Sm_2Zr_2O_7$-S was 2.12, 2.113, 2.097, and 2.088 at 0.2 C, 0.5 C, 1 C, 2 C, respectively, while high discharge plateau voltage was 2.342, 2.319, 2.279, and 2.256, respectively. Low discharge plateau voltage of ZrO_2-S was 2.091, 2.072, 2.058, and 2.043 V at 0.2 C, 0.5 C, 1 C, 2 C, respectively, while high discharge plateau voltage was 2.317, 2.273, 2.221, and 2.185 V, respectively.

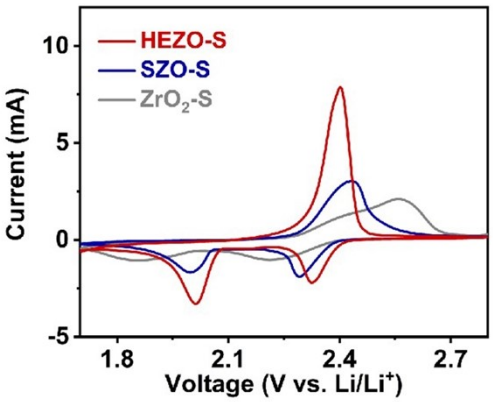

Figure S22. CV curves of HEZO-S, $Sm_2Zr_2O_7$-S, ZrO_2-S cathodes.

The observed pairs of peaks on the redox scanning curves belong to the lithiation of S and the decomposition of Li_2S. During the reduction process, the current density at the maximum reduction peak and its corresponding potential for HEZO-S are 1.02 mA cm^{-2} (at 2.33 V) and 1.47 mA cm^{-2} (at 2.01 V), respectively. In the oxidation decomposition of Li_2S, the current density at the maximum oxidation peak was 3.33 mA cm^{-2}, and the corresponding potential was 2.40 V. For the $Sm_2Zr_2O_7$-S composite, the current density at the maximum reduction peak was 0.88 mA cm^{-2} (at 2.28 V) and 0.75 mA cm^{-2} (at 1.99 V), respectively. During the oxidation, the current density at the maximum reduction peak is 1.32 mA cm^{-2} (at 2.43 V). The ZrO_2-S composite exhibits a current density of 0.49 mA cm^{-2} (at 2.20 V) and 0.62 mA cm^{-2} (at 1.86 V) at the maximum reduction peak, while the current density at the maximum oxidation peak was 0.93 mA cm^{-2}, and the corresponding potential was 2.56 V. Furthermore, the differential cyclic voltammetry curves were analyzed to accurately compare the initial potentials of the electrochemical conversion reactions. For the reduction reaction, the initial potentials of the HEZO-S electrode were 2.45 V and 2.08 V, while for the oxidation reaction, the initial potential is 2.15 V. In comparison, the initial potentials of the $Sm_2Zr_2O_7$-S electrode for the reduction reaction were 2.40 V and 2.06 V, and the initial potential was 2.22 V for the oxidation reaction. The ZrO_2-S electrode has initial potentials of 2.37 V and 2.03 V for the reduction reaction, and 2.27 V for the oxidation reaction. Comparatively, the HEZO-S composite exhibits a negative shift in both the maximum and onset potentials during S reduction and Li_2S oxidation, indicating its enhanced electrocatalytic activity.

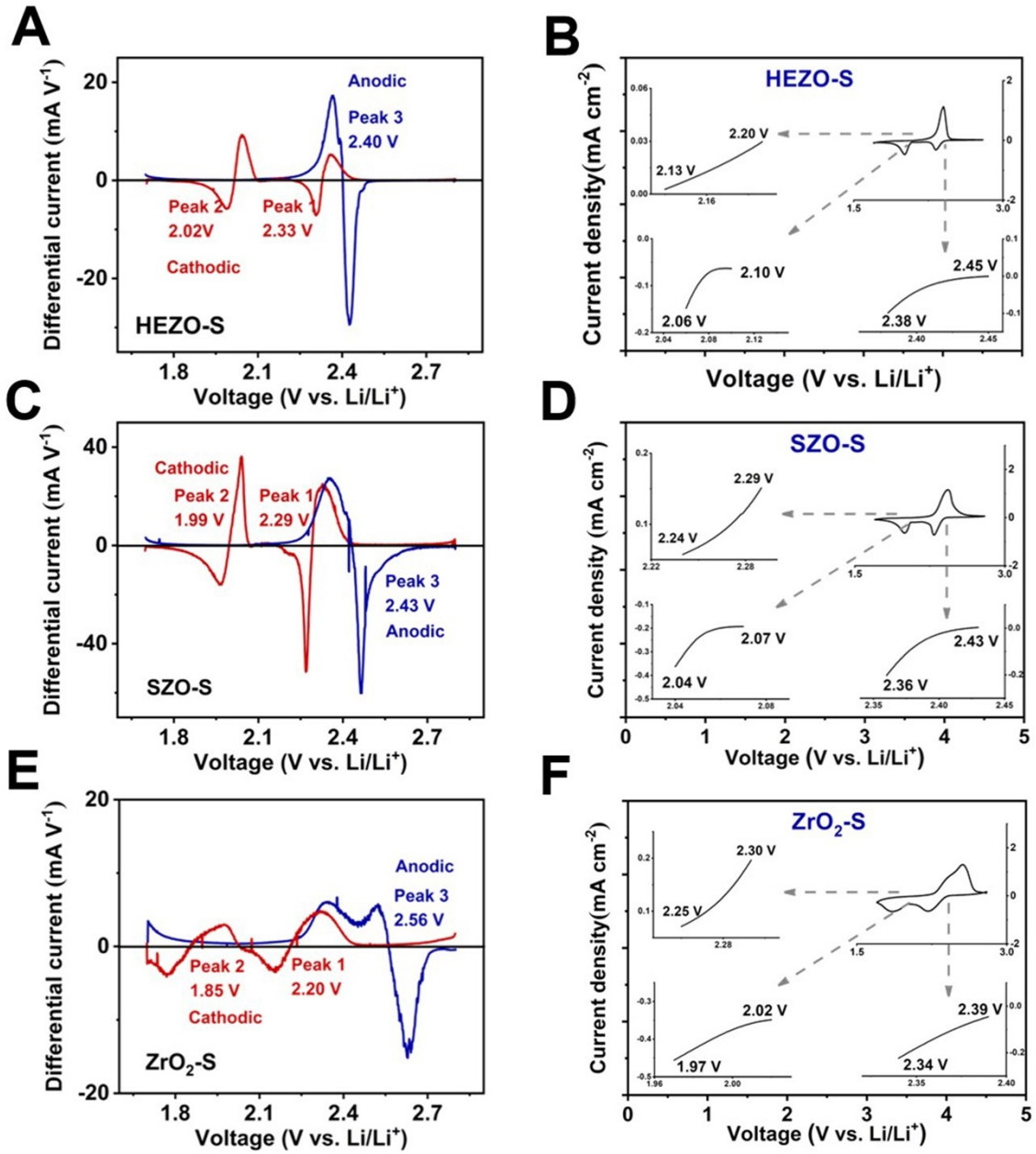

Figure S23. A, Differential CV curves of HEZO-S. **B,** CV curves and corresponding onset potentials of redox peaks of HEZO-S. **C,** Differential CV curves of $Sm_2Zr_2O_7$-S. **D,** CV curves and corresponding onset potentials of redox peaks of $Sm_2Zr_2O_7$-S. **E,** Differential CV curves of ZrO_2-S. **F,** CV curves and corresponding onset potentials of redox peaks of ZrO_2-S.

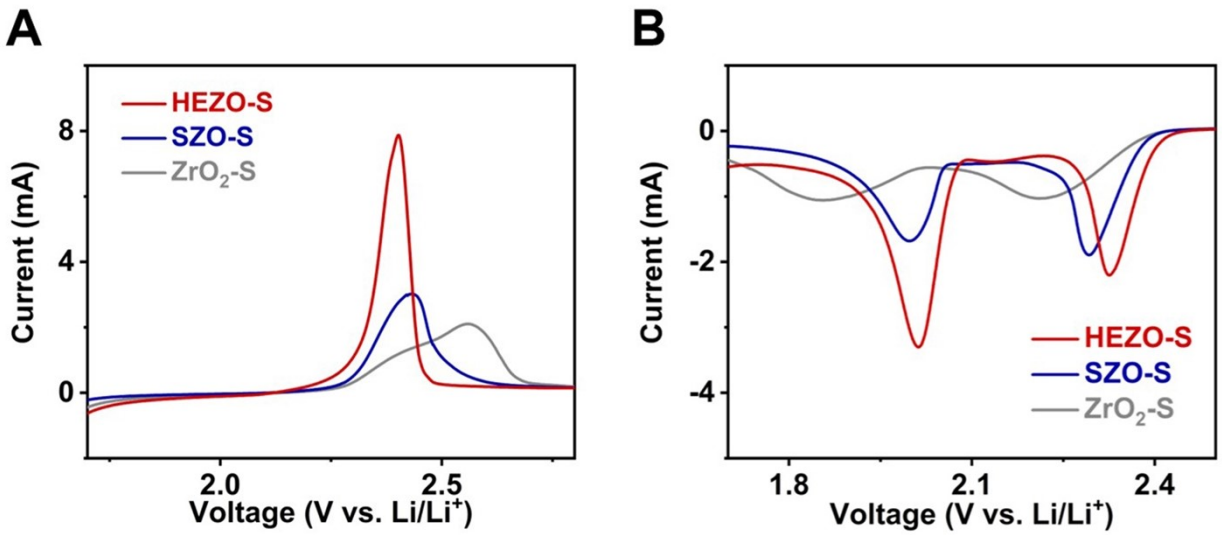

Figure S24. Linear voltammetry curve of HEZO-S, $Sm_2Zr_2O_7$-S, ZrO_2-S cathodes **A,** Charge progress. **B,** discharge progress.

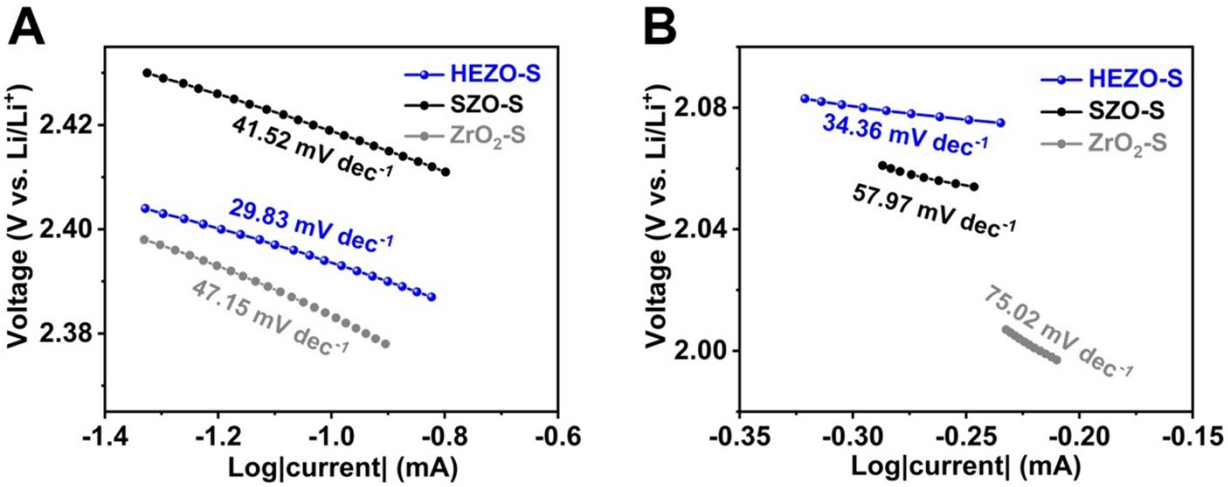

Figure S25. Tafel plots of HEZO-S, $Sm_2Zr_2O_7$-S, ZrO_2-S cathodes **A,** Reduction peak I. **B,** Reduction peak II.

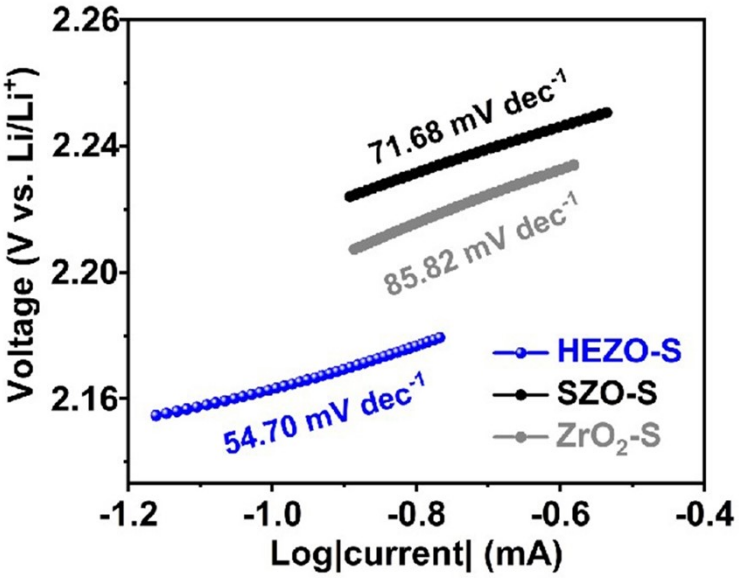

Figure S26. Tafel plots of HEZO-S, $Sm_2Zr_2O_7$-S, and ZrO_2-S cathodes during the oxidation peak.

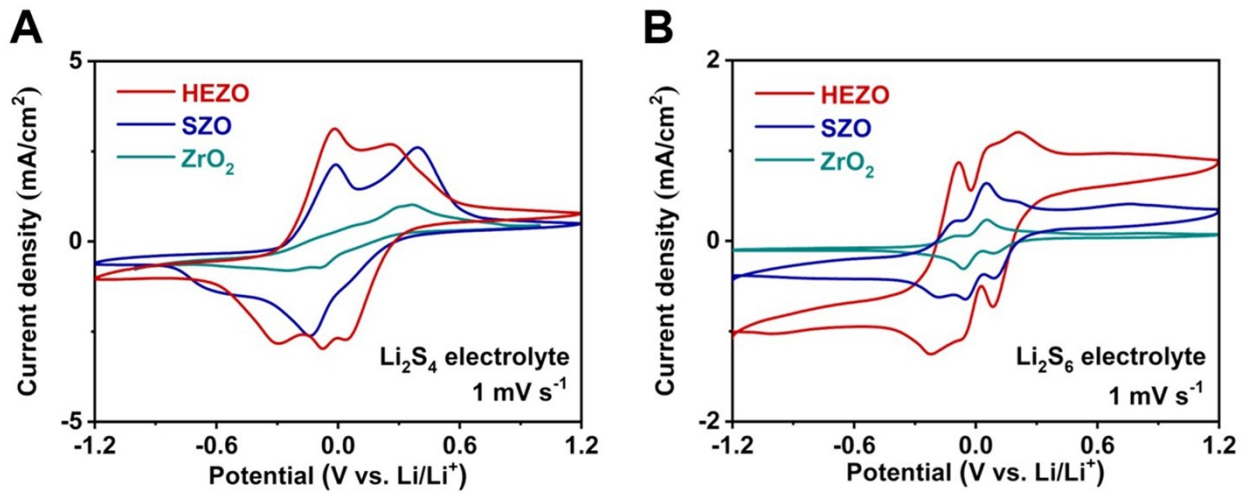

Figure S27. A, CV curves of Li_2S_4 catholyte symmetric cells for HEZO / Li_2S_4/ HEZO, $Sm_2Zr_2O_7$ / Li_2S_4/ $Sm_2Zr_2O_7$, and ZrO_2 / Li_2S_4/ ZrO_2 electrodes. **B,** CV curves of Li_2S_6 catholyte symmetric cells for HEZO / Li_2S_6/ HEZO, $Sm_2Zr_2O_7$ / Li_2S_6/ $Sm_2Zr_2O_7$, and ZrO_2 / Li_2S_6/ ZrO_2 electrodes.

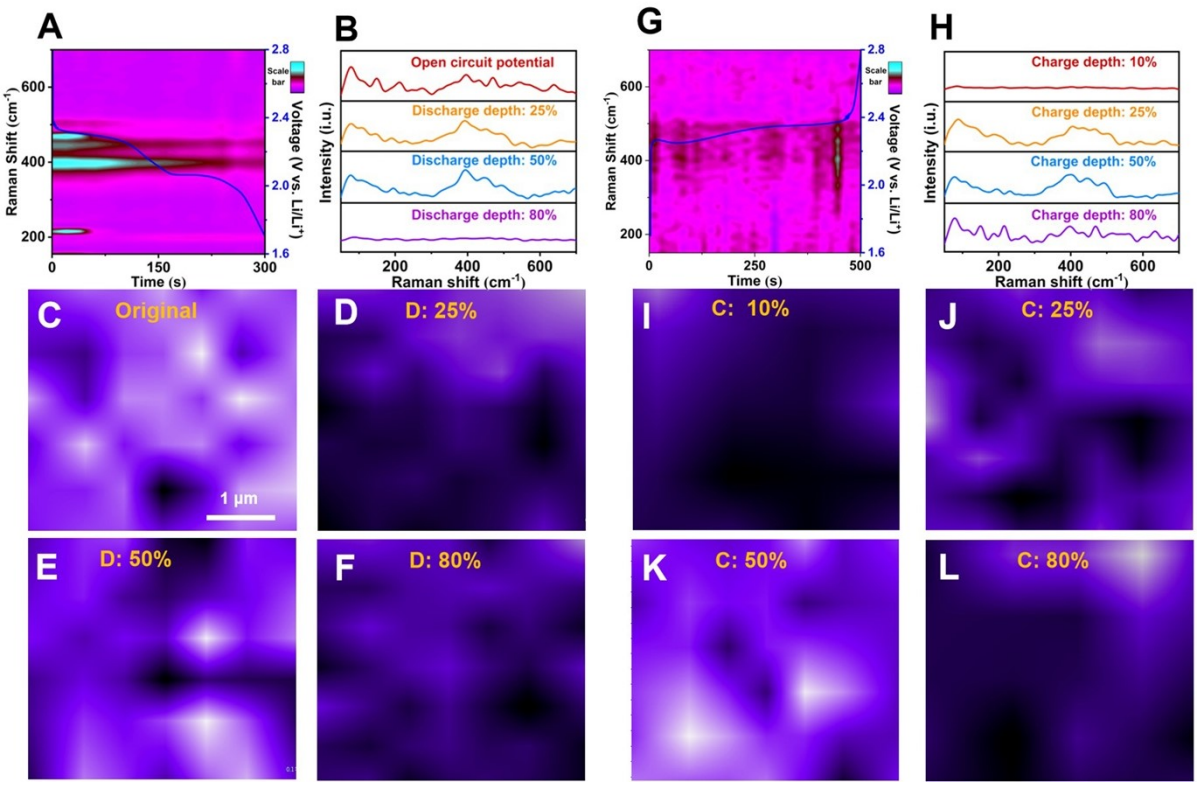

Figure S28. $Sm_2Zr_2O_7$-S cathode. **A,** Time sequence of Raman spectra obtained during the discharge progress. **B,** *In-situ* cell at OCP, the depth of discharge is 25%, 50% and 80% of the Raman signal. Deconvolution of *in-situ* confocal Raman mapping signals spectra with different discharge states of **C,** open-circuit potential, **D,** discharge depth 25%, **E,** discharge depth 50%, and **F,** discharge depth 80%. **G,** Time sequence of Raman spectra obtained during the charge progress. **H,** *In-situ* cell at OCP, the depth of charge is 10%, 25%, 50% and 80% of the Raman signal. Deconvolution of *in-situ* confocal Raman mapping signals spectra with different discharge states of **I,** charge depth 10%, **J,** charge depth 25%, **K,** charge depth 50%, and **L,** charge depth 80%.

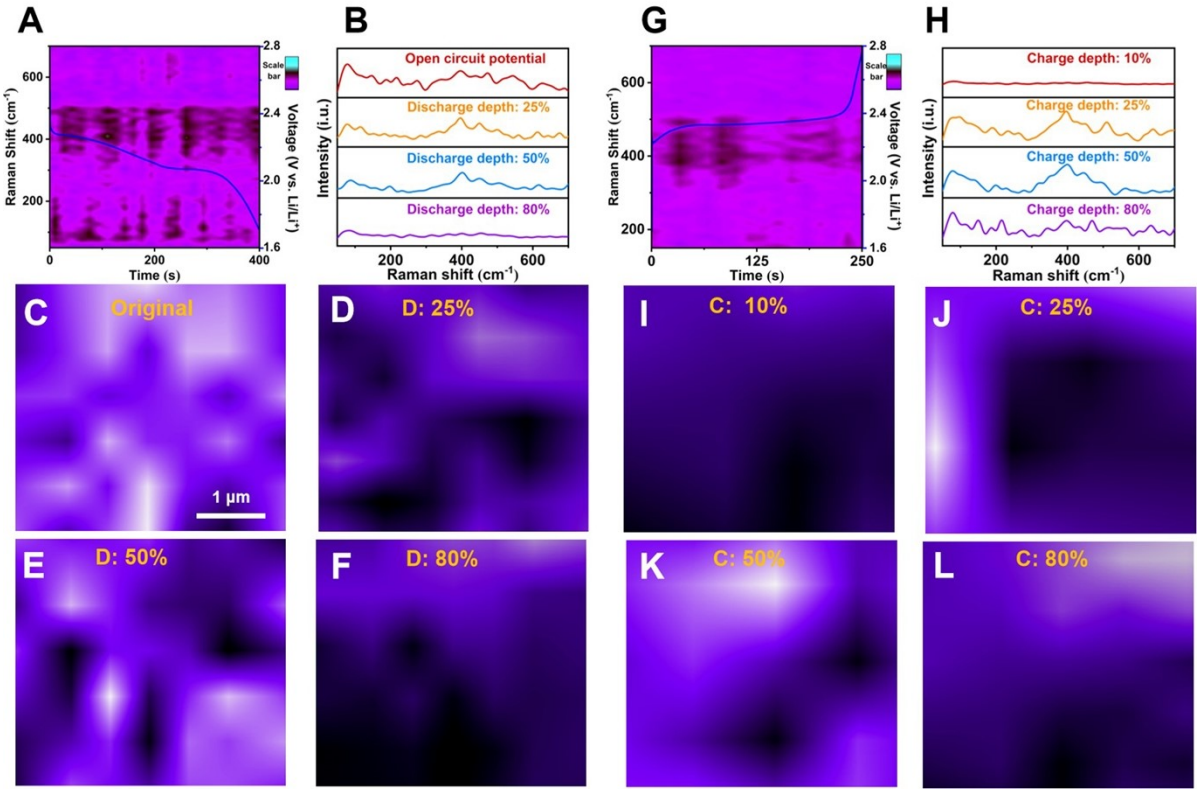

Figure S29. ZrO_2-S cathode. **A,** Time sequence of Raman spectra obtained during the discharge progress. **B,** *In-situ* cell at OCP, the depth of discharge is 25%, 50% and 80% of the Raman signal. Deconvolution of *in-situ* confocal Raman mapping signals spectra with different discharge states of **C,** open-circuit potential, **D,** discharge depth 25%, **E,** discharge depth 50%, and **F,** discharge depth 80%. **G,** Time sequence of Raman spectra obtained during the charge progress. **H,** *In-situ* cell at OCP, the depth of charge is 10%, 25%, 50% and 80% of the Raman signal. Deconvolution of *in-situ* confocal Raman mapping signals spectra with different discharge states of **I,** charge depth 10%, **J,** charge depth 25%, **K,** charge depth 50%, and **L,** charge depth 80%.

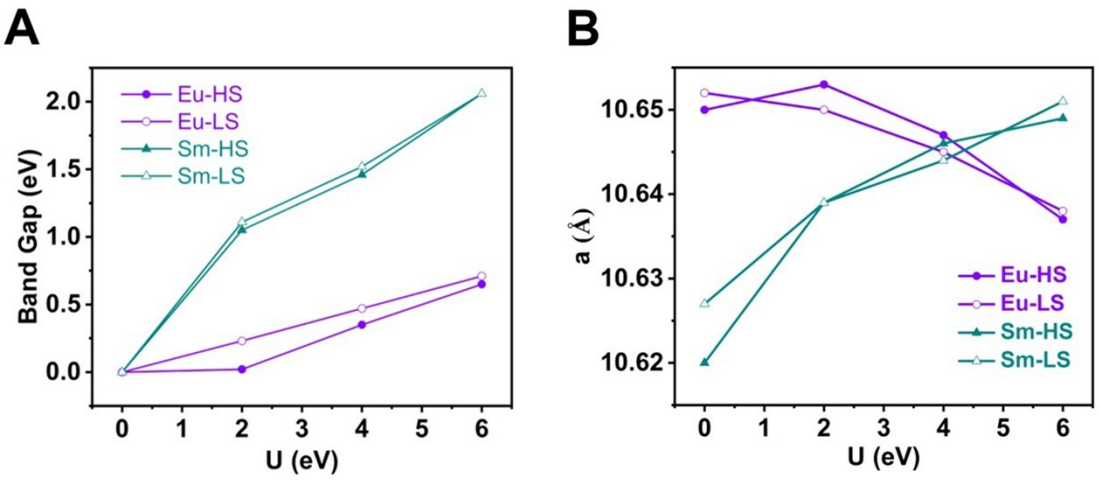

Figure S30. A, The band gap of crystal and the distribution of fine intermediate energy level of orbital in the forbidden band. **B,** The change of lattice size when different U values are applied to the f orbital.

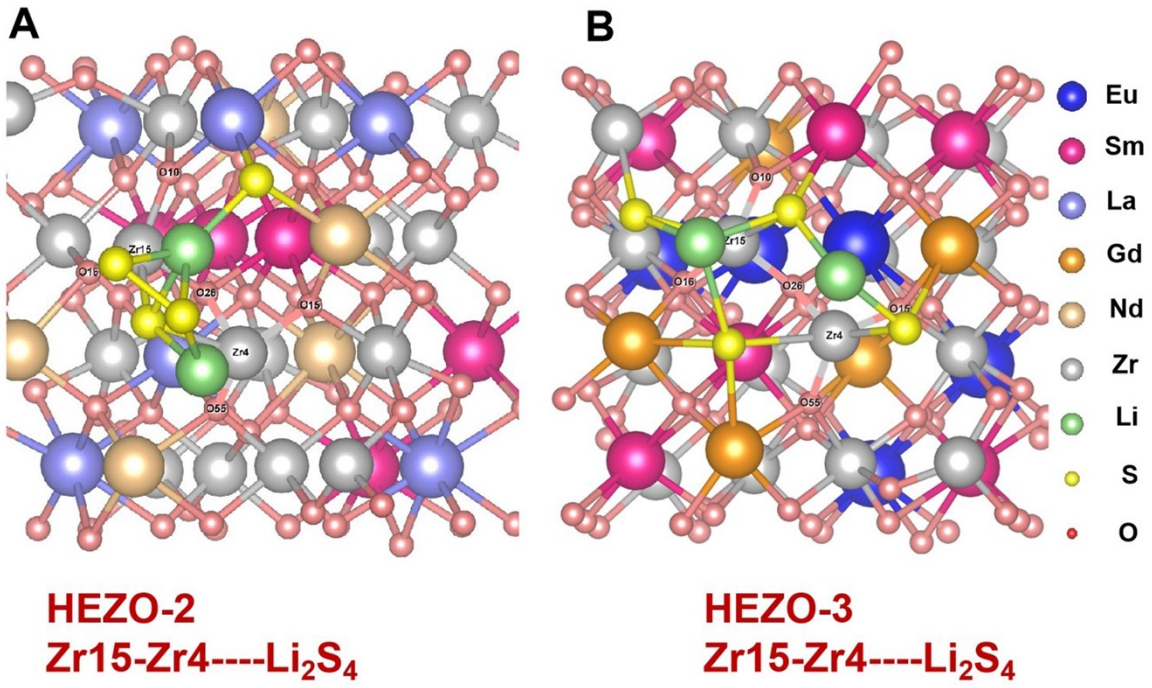

Figure S31. A, The adsorption configuration diagram without oxygen vacancy of Li_2S_4 at the Zr site on the (100) crystal surface of HEZO-2. **B,** The adsorption configuration diagram without oxygen vacancy of Li_2S_4 at the Zr site on the (100) crystal surface of HEZO-3.

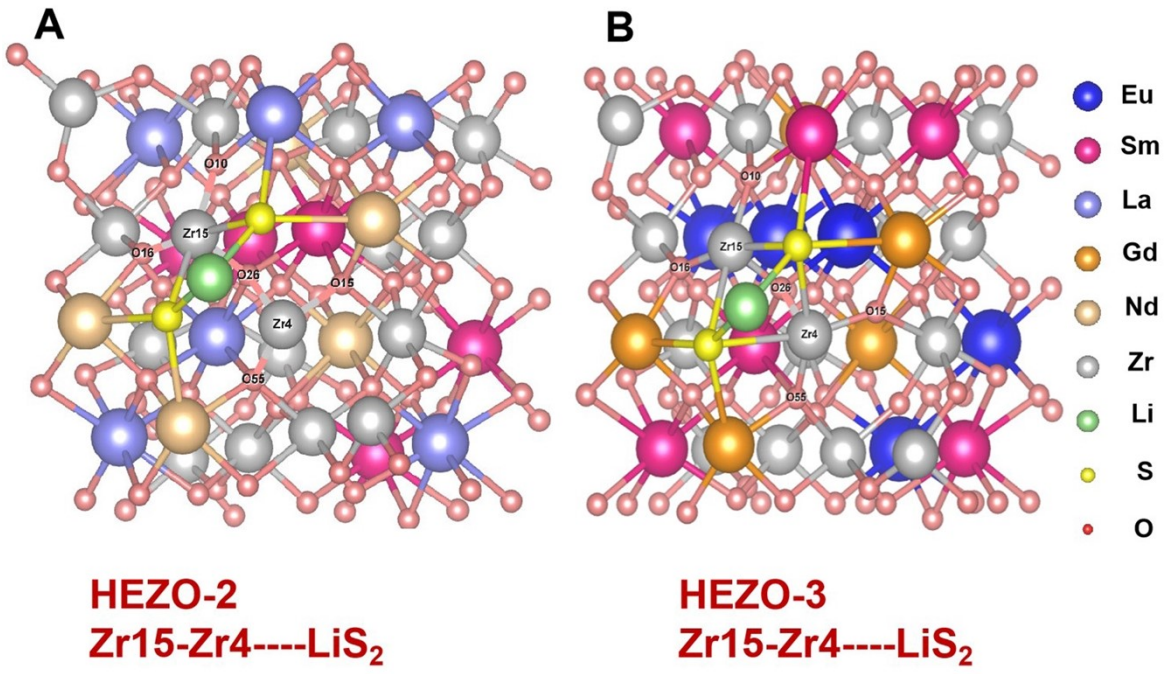

Figure S32. A, The adsorption configuration diagram without oxygen vacancy of LiS_2 at the Zr site on the (100) crystal surface of HEZO-2. **B,** The adsorption configuration diagram without oxygen vacancy of LiS_2 at the Zr site on the (100) crystal surface of HEZO-3.

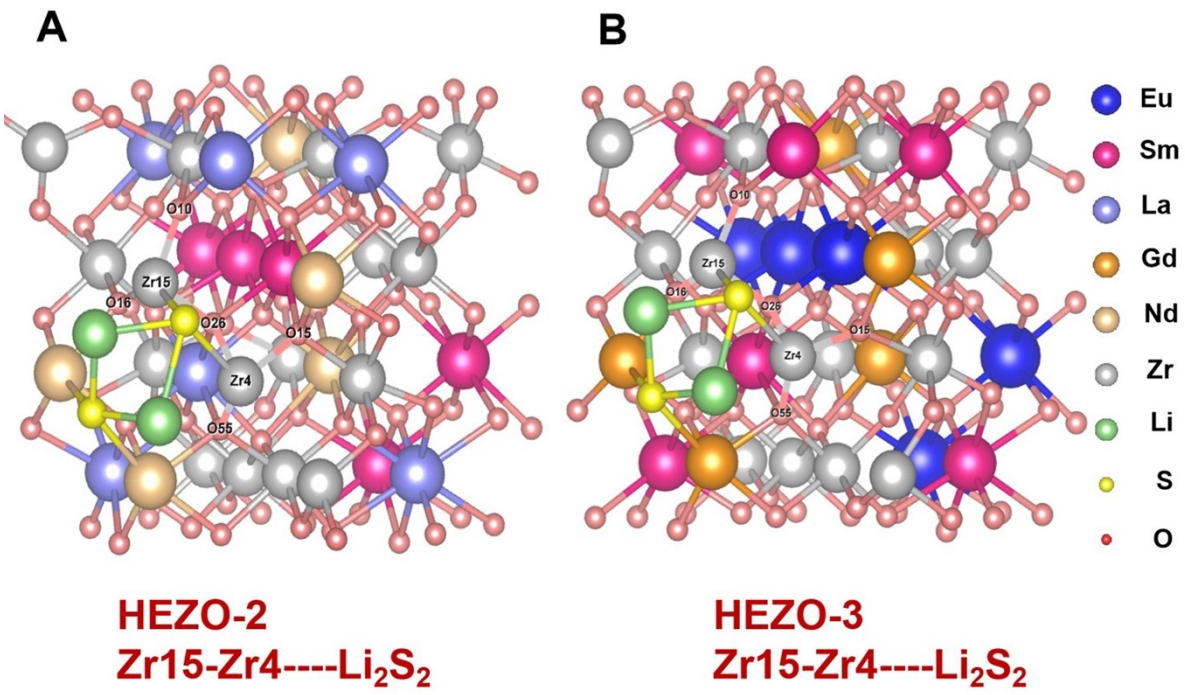

Figure S33. A, The adsorption configuration diagram without oxygen vacancy of Li_2S_2 at the Zr site on the (100) crystal surface of HEZO-2. **B,** The adsorption configuration diagram without oxygen vacancy of Li_2S_2 at the Zr site on the (100) crystal surface of HEZO-3.

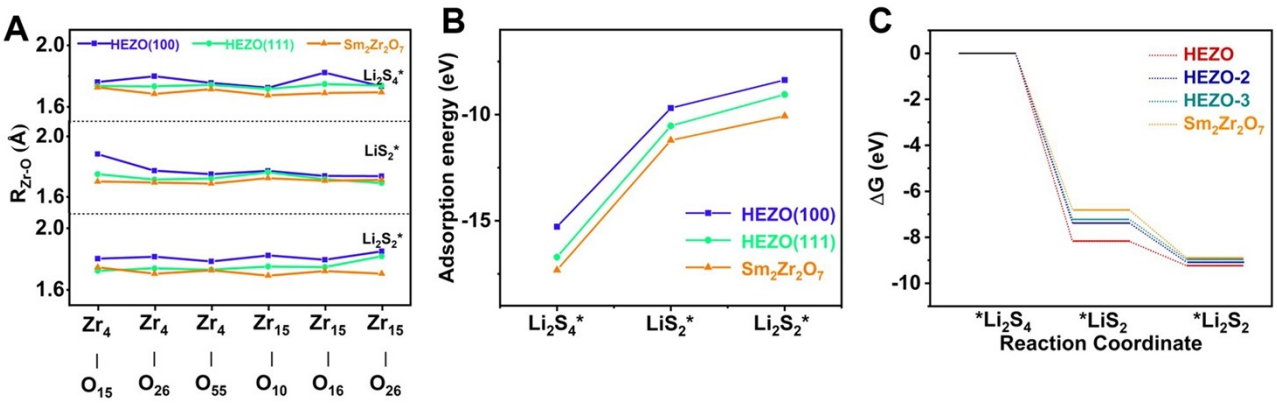

Figure S34. A, The length of the Zr-O bond at the Zr site of (100) and (111) crystal face without oxygen vacancy under three adsorption states in the transformation of Li_2S_4. **B,** Adsorption energy at Zr site of (100) and (111) crystal face without oxygen vacancy in three adsorption states. **C,** Gibbs free energy diagram of Li_2S_4 conversion steps of HEZO and $Sm_2Zr_2O_7$ substrate without oxygen vacancy.

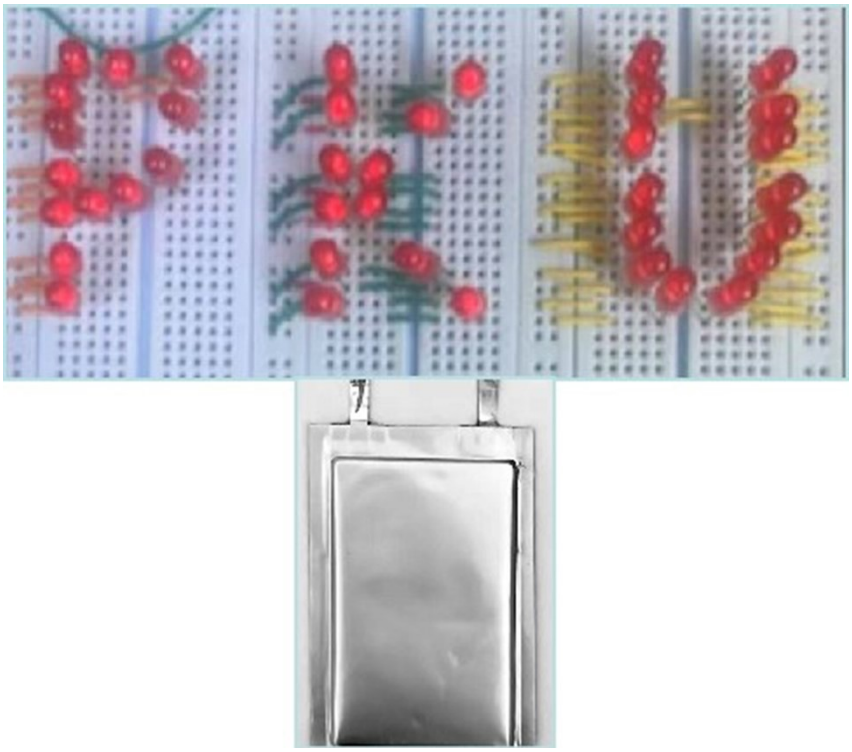

Figure S35. The performance of the pouch battery is shown after 100 cycles.

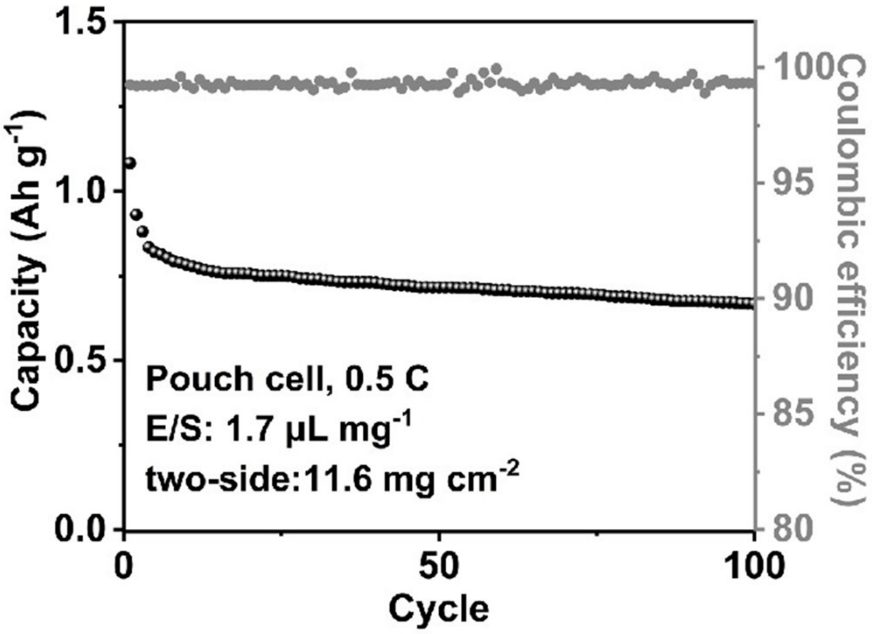

Figure S36. Double-sided high load capacity, low E/S ratio HEZO-S pouch cell performance.

Reference

[S1] ORaza, H., et al., High-entropy stabilized oxides derived via a low-temperature template route for high-performance lithium-sulfur batteries. *EcoMat* **5**, e12324 (2023).

[S2] Du, M., et al., High-entropy Prussian blue analogues and their oxide family as sulfur hosts for lithium-sulfur batteries. *Angew. Chem. Int. Ed.* **61**, e202209350 (2022).

[S3] Tian, L., et al., High-entropy perovskite oxide nanofibers as efficient bidirectional electrocatalyst of liquid-solid conversion processes in lithium-sulfur batteries. *Nano Energy* **106**, 108037 (2023).

[S4] Ma, Y., et al., High-Entropy Metal Oxide-Coated Carbon Cloth as Catalysts for Long-Life Li–S Batteries. *Langmuir* **40**, 11626-11634 (2024).

[S5] Cai, Z., et al., Lithium-rich high entropy oxide with abundant oxygen vacancies for composite polymer all-solid-state Li-S batteries. *Chem. Eng. J.* **499**, 156000 (2024).

[S6] Li, G. R. et al. Polysulfide regulation by the zwitterionic barrier toward durable lithium–sulfur batteries. *J. Am. Chem. Soc.* **142**, 3583 (2020).

[S7] Liu, Y.-T., Liu, S., Li, G.-R., Yan T.-Y. & Gao, X.-P. High volumetric energy density sulfur cathode with heavy and catalytic metal oxide host for lithium–sulfur battery. *Adv. Sci.* **7**, 1903693 (2020).

[S8] Monisha, M. et al. Halogen-free flame-retardant sulfur copolymers with stable Li–S battery performance. *Energy Storage Mater.* **29**, 350 (2020).

[S9] Shi, H. D. et al. Interfacial engineering of bifunctional niobium (V)-based heterostructure nanosheet toward high efficiency lean-electrolyte lithium–sulfur full batteries. *Adv. Funct. Mater.* **31**, 2102314 (2021).

[S10] Hou, W. et al. Catalytic mechanism of oxygen vacancies in perovskite oxides for lithium–sulfur batteries. *Adv. Mater.* **34**, 2202222 (2022).

[S11] Zou, K. Y. et al. Facilitating catalytic activity of indium oxide in lithium-sulfur batteries by controlling oxygen vacancies. *Energy Storage Mater.* **48**, 133-144 (2022).

[S12] Liu, F.-J. et al. Cation-doped V_2O_5 microsphere as a bidirectional catalyst to activate sulfur redox reactions for lithium-sulfur batteries. *Chem. Eng. J.* **456**, 140948 (2023).

[S13] Ma, L. et al. Integrating energy band alignment and oxygen vacancies engineering of TiO_2 anatase/rutile homojunction for kinetics-enhanced Li–S batteries. *Adv. Funct. Mater.* **33**, 2305788 (2023).

[S14] Fu, S. N. et al. Tuning the crystalline and electronic structure of ZrO_2 via oxygen vacancies and nano-structuring for polysulfides conversion in lithium-sulfur batteries. *J. Energy Chem.* **88**, 82-93 (2024).

[S15] Wang, S. Z. et al. Immobilizing polysulfide via multiple active sites in $W_{18}O_{49}$ for Li-S batteries by oxygen vacancy engineering. *Energy Storage Mater.* **43**, 422-429 (2021).

[S16] Fang, D. L. et al. Combination of heterostructure with oxygen vacancies in Co@ CoO_{1-x} nanosheets array for high-performance lithium sulfur batteries. *Chem. Eng. J.* **411**, 128546 (2021).

[S17] Chung, S. H. et al. High entropy oxide $(CrMnFeNiMg)_3O_4$ with large compositional Space shows long-term stability as cathode in lithium-sulfur batteries. *ChemSusChem* 16, e202300135 (2023).

[S18] Li, H. T. et al. Cooperative catalysis of polysulfides in lithium-sulfur batteries through adsorption competition by tuning cationic geometric configuration of dual-active sites in spinel oxides. *Angew. Chem. Int. Ed.* **8**, e202216286 (2023).

[S19] Yu, Y. J. et al. Manganese oxide nanosheets with mixed valence states as a separator coating for lithium–sulfur batteries. *ACS Applied Energy Mater.* **6**, 7298-7304 (2023).

[S20] Li, C. C. et al. Manipulating electrocatalytic polysulfide redox kinetics by 1D core–shell like composite for lithium–sulfur batteries. *Adv. Energy Mater.* **12**, 2103915 (2022).

[S21] Li, Y. J. et al. Manipulating redox kinetics of sulfur species using Mott–Schottky electrocatalysts for advanced lithium–sulfur batteries. *Nano Lett.* **21**, 6656-6663 (2021).

[S22] Sun, R. et al. Enhancing polysulfide confinement and electrochemical kinetics by amorphous cobalt phosphide for highly efficient lithium–sulfur batteries. *ACS Nano* **15**, 739-750 (2021).

[S23] Yang, B. Z. et al. Binder-Free ω-$Li_3V_2O_5$ Catalytic Network with Multi-Polarization Centers Assists Lithium–Sulfur Batteries for Enhanced Kinetics Behavior. *Adv. Funct. Mater.* **32**, 2110665 (2022).

[S24] Qian, J. et al. Enhanced electrochemical kinetics with highly dispersed conductive and electrocatalytic mediators for lithium–sulfur batteries. *Adv. Mater.* **33**, 2100810 (2021).

[S25] Wang, L. et al. Design rules of a sulfur redox electrocatalyst for lithium–sulfur batteries. *Adv. Mater.* **34**, 2110279 (2022).

[S26] Liu, Y. N. et al. O-, N-Coordinated single Mn atoms accelerating polysulfides transformation in lithium-sulfur batteries. *Energy Storage Mater.* **35**, 12-18 (2021).

[S27] Qu, W. J. et al. Targeted catalysis of the sulfur evolution reaction for high-performance lithium-sulfur batteries. *Adv. Energy Mater.* **12**, 2202232 (2022).

[S28] Zeng, Q. H. et al. Copolymerization of sulfur chains with vinyl functionalized metal− organic framework for accelerating redox kinetics in lithium− sulfur batteries. *Adv. Energy Mater.* **12**, 2104074 (2022).

[S29] Wang, X. B. et al. Creating edge sites within the 2D metal-organic framework boosts redox kinetics in lithium–sulfur batteries. *Adv. Energy Mater.* **12**, 2201960 (2022).

[S30] Jiang, Y. C., Liu, S., Gao X. P. & Li, G. R. Morphology control of Li_2S deposition via geometrical effect of cobalt-edged nickel alloy to improve performance of lithium–sulfur batteries. *Adv. Funct. Mater.* **33**, 2304965 (2023).

[S31] Li, Z. N. et al. Lithiated metallic molybdenum disulfide nanosheets for high-performance lithium–sulfur batteries. *Nature Energy* **8**, 84-93 (2023).

[S32] Wang, J. Y. et al. Engineering the conductive network of metal oxide-based sulfur cathode toward efficient and longevous lithium–sulfur batteries. *Adv. Energy Mater.* **10**, 2002076 (2020).

[S33] Liu, J. B. et al. Design zwitterionic amorphous conjugated micro-/mesoporous polymer assembled nanotentacle as highly efficient sulfur electrocatalyst for lithium-sulfur batteries. *Adv. Energy Mater.* **11**, 2101926 (2021).

[S34] Chen, L. P. et al. Bifunctional catalytic effect of $CoSe_2$ for lithium–sulfur batteries: single doping versus dual doping. *Adv. Funct. Mater.* **32**, 2107838 (2022).

[S35] Yang, J.-L. et al. Rich heterointerfaces enabling rapid polysulfides conversion and regulated Li_2S deposition for high-performance lithium–sulfur batteries. *ACS Nano* **15**, 11491-11500 (2021).